Engineering the electronic structure of isolated manganese sites to improve the oxygen reduction, Zn-air battery and fuel cell performances

Xue Bai [a,1], Yin Wang [c,1], Jingyi Han [a], Xiaodi Niu [b,*], Jingqi Guan [a,*]

[a] *Institute of Physical Chemistry, College of Chemistry, Jilin University, 2519 Jiefang Road, Changchun 130021, PR China*
[b] *College of Food Science and Engineering, Jilin University, Changchun 130062, PR China*
[c] *Inner Mongolia Key Laboratory of Carbon Nanomaterials, Nano Innovation Institute (NII), College of Chemistry and Materials Science, Inner Mongolia Minzu University, Tongliao 028000, PR China*

ABSTRACT

Single-atom manganese catalysts possess high stability in the oxygen reduction reaction (ORR) due to their lower Fenton reaction activity. Here, we employ N- and S-co-coordination strategy to modulate the microstructural Mn sites towards high-efficiency ORR. The fabricated Mn-N/S-C catalyst with isolated $Mn-N_2S_2$ sites demonstrates a positive half-wave potential of 0.91 V for the ORR. The fabricated zinc–air battery with Mn-N/S-C as the cathode affords a maximal power density of 193 mW cm^{-2} and superior output stability. Moreover, the maximal power density is increased by 1.53 times compared with S-free Mn-N-C catalyst in anion exchange membrane fuel cells (AEMFCs). Both experimental characterizations and theoretical simulations unveil that the main active sites in the Mn-N/S-C should be $Mn-N_2S_2$ moiety embedded into the graphene framework ($Mn-N_2S_2G$). Further computational results demonstrate that the S atom doping and asymmetry of structure lead to higher ORR activities of ortho-$Mn-N_2S_2G$ than $Mn-N_4G$, $Mn-N_3SG$, para-$Mn-N_2S_2G$ and $Mn-NS_3G$.

1. Introduction

Advanced metal-air batteries with high theoretical energy density have been considered as an environmentally-friendly and high-efficiency energy technology [1,2], while hydrogen fuel cells with zero carbon emissions have the advantages of high conversion efficiency, large capacity, high specific energy, wide power range and no charging, which are a promising new power source [3]. Although the overall performance of fuel cells and metal-air batteries are impacted by different parameters, their capability is seriously perplexed by the slow dynamics of the oxygen electrode reaction [4,5]. Different from proton exchange membrane fuel cells (PEMFCs), AEMFCs are operated in basic environments, which allow the use of non-precious metal catalysts, thus exhibiting great hope to reduce costs [6]. Although platinum-group materials show excellent ORR performance, the scarce and expensive resource reserve of the precious metals have hindered the extensive application [7,8]. Therefore, it is urgent to explore high-performance non-precious metal ORR catalysts for the applications of metal-air batteries and fuel cells [9,10].

Owing to the maximized atom utilization and high intrinsic activity,

single-atom catalysts (SACs) have shown extensive application prospects in electrocatalytic field [11,12]. Especially, Fe-/Co-N-C catalysts exhibit outstanding ORR activity [13–17]. Nevertheless, these electrocatalysts are insufficiently durable at high voltages, resulting from the structural damage of atomic metal sites, which restricts their practical applications in metal-air batteries [18,19]. The Fe-N-C electrocatalysts promotes the Fenton reactions, where active free radicals (HO·, HOO·) will be produced, which can attack and destroy the M-N bonds and the polymer membrane [20]. Alternatively, atomic Mn-N-C catalysts display theoretically higher durability than Fe-N-C catalysts in harsh oxidation environment due to lower formation energy of $Mn-N_4$ sites than $Fe-N_4$ sites [21]. Hence, atomic Mn-N-C catalysts have drawn intensive research attention for the ORR in recent years. For instance, Li et al. prepared an atomic Mn-N-C catalyst with $Mn-N_4$ active centers, which displayed a half-wave potential ($E_{1/2}$) of 0.8 V in acidic media [20]. Wu et al. converted core–shell MnO_2@ZIF-8 nanowires into Mn-based catalysts with $Mn-N_2$ and $Mn-N_4$ configurations, and found that the latter exhibited better ORR performance than the former [22]. Liu et al. characterized the Mn-N-C catalysts by in situ X-ray absorption spectroscopy (XAS) and concluded that the low-valence $Mn^{\delta+}-N_4$ is the ORR

---

active site [23]. Despite single-atom manganese catalysts have made rapid progress in the ORR field, the catalytic performance is still insufficient for existing applications, which requires us to further optimize the electronic structure of Mn sites.

The geometric construction and electronic structure of M-N-C can be modulated by doping with alien atoms such as oxygen, sulfur, phosphorus, etc., which would further promote the electrocatalytic performance [12,24]. For instance, Chen et al. fabricated a Mn/C-NO catalyst with Mn-N$_3$O$_1$ site by annealing Mn-1,3,5-benzenetricarboxylic acid under N$_2$ followed by HCl etching and ammonia activation, which displayed a power density of ~120 mW cm^{-2} as the cathode catalyst in a zinc-air cell [25]. Wang et al. prepared a Fe-SAs/NSC electrocatalyst with well-dispersed Fe-N$_4$S$_2$ center sites, showing a more positive E$_{1/2}$ (0.87 V) than Co-SAs/NSC with Co-N$_3$S$_1$ sites and Ni-SAs/NSC with Ni-N$_3$S$_1$ sites. [26] Li et al. fabricated a multiaperture Cu SAC with Cu-N$_3$S$_1$ sites and low-valence Cu^{1+} species, which exhibited E$_{1/2}$ of 0.918 V [27]. Thus, double nonmetallic modulation strategy is very efficient to modify the metallic electronic structure and further increase the electrocatalytic activity [28].

Herein, we anchor isolated single-atom Mn sites onto N/S-codoped graphene (Mn-N/S-C). The Mn-N/S-C delivers high ORR activity (E$_{1/2}$ = .91 V), which is superior to Mn-C, Mn-S-C, Mn-N-C catalysts and even commercial Pt/C catalysts in alkaline media. Structural characterizations and theoretical simulations show that the ortho-Mn-N$_2$S$_2$G configuration exhibits higher ORR activity than Mn-N$_4$G, Mn-N$_3$SG, para-Mn-N$_2$S$_2$G and Mn-NS$_3$G configurations due to the asymmetry of structure resulting from S atom doping.

2. Experimental methods

2.1. Catalyst preparation

Mn^{2+} ions were first adsorbed onto graphene oxide (GO) by freeze drying of the Mn^{2+}/GO mixture, where the mass ratio of Mn: GO is 0.5: 100. Here, the abundant hydroxyl and carboxyl groups of GO coordinate manganese cations to guarantee well dispersion. The obtained Mn^{2+}/GO powder was mixed with sulfur, urea, and thiourea, and then annealed at 800 °C under nitrogen atmosphere to produce Mn-S-C, Mn-N-C, and Mn-N/S-C (or 0.7%Mn-N/S-C-800), respectively. Mn-C was obtained by annealing the Mn^{2+}/GO at 800 °C under the protection of nitrogen. For comparison, *c*-Mn-N/S-C-*T* with different manganese content (*c* = 0.3, 0.5, 0.7, or 0.9 wt%) and different annealing temperature (*T* = 700, 800, or 900 °C) were also synthesized using an analogous synthetic procedure.

2.2. Material characterizations

X-ray diffraction (XRD) was conducted on a Shimadzu XRD-6000. Transmission electron microscope (TEM) was performed on a Hitachi HT7700. High angle annular dark field imaging (HAADF) was conducted on a JEM-ARM 200 F microscope. X-ray photoelectron spectroscopy (XPS) spectra were conducted on a Thermo VG ESCALAB 250. XAS spectrum of Mn-N/S-C at Mn K edge was conducted at BL14W1 beamline of Shanghai Synchrotron Radiation Facility.

2.3. Electrochemical activity characterizations

Electrochemical experiments were performed in 0.1 M KOH on an electrochemical workstation (CHI760e) coupled with a rotating disk electrode (RDE) system, contain a saturated Hg/Hg$_2$Cl$_2$ electrode and a carbon rod as the reference electrode and counter electrode, respectively. The catalyst loading on the RDE is 0.5 mg cm^{-2}. The number of electron transfer (n) determined by the slopes of the lines is calculated by the K-L equation [29]. The H$_2$O$_2$ yield and electron transfer number from rotating ring-disk electrode measurements are calculated by Eqs. (1) and (2):

$$n = \frac{4 * |i_d|}{i_r/N + i_d} \tag{1}$$

$$HO_2^-(\%) = 200 * \frac{i_r/N}{i_r/N + i_d} \tag{2}$$

where i$_d$ and i$_r$ is disk current and ring current, respectively, and N = 0.4 is the current collection efficiency of the Pt ring. All potentials were transformed to the reversible hydrogen electrode (RHE) by Nernst formula: E$_{RHE}$ = E$_{SCE}$ + 0.241 V + 0.0591 pH.

2.4. Zn-air battery tests

The Zn-air battery performances were evaluated in 6 M KOH on a battery test system (LANHE CT2001A). The modified carbon paper (catalyst loading: 1 mg cm^{-2}) and a Zn plate (1 mm in thickness) were used as the air electrode and the metal electrode, respectively.

2.5. H$_2$/O$_2$ fuel cell tests

QPCTP-10 polymer with 20 μm thickness was used as the AEM [30], 75 % PtRu/C was used as the anode catalyst, and Mn-N-C or Mn-N/S-C was served as the cathode catalyst. The ionomer solution (5 wt%) was prepared by dissolving QPCBP-10 polymer into dimethyl sulfoxide solution. Then, the mixture of catalyst and ionomer with mass ratio of 3.5/1 was added into a solution of isopropanol/deionized water (9/1) to form a catalyst ink by ultrasonic treatment. Subsequently, it was sprayed onto the AEM with the anode loading mass of 0.4 mg cm^{-2} and the cathode loading mass of 1.5 mg cm^{-2}. The as-prepared AEM was soaked into 1 M NaOH at 60 °C for 24 h, which was then positioned between two pieces of carbon paper (HCP120) under the pressure of 0.1 MPa to obtain the membrane electrode assembly (MEA). Finally, the MEA was placed in a fuel cell test system (850e Multi Range, Scribner Associates Co.) to test the performance. The effective area was 5 cm^{-2}. The fuel cell was tested at 80 °C. The humidified temperatures for the anode and cathode were 73 °C and 80 °C, respectively.

2.6. Computational methods

Density functional theory (DFT) calculations were performed using Vienna ab initio simulation package (VASP) software [31,32]. In this work, the proposed ORR mechanism involves *OOH, *O and *OH intermediates. The graphene supercell with surface periodicity of 6 × 6 containing 71 atoms was constructed. The convergence threshold was appointed as 1 × 10^{-4} eV in total energy and 0.05 eV/Å on each atom. The charge density difference of Mn-N$_x$S$_x$G was calculated by using VASPKIT software [33]. Firstly, the structures of Mn-N$_x$S$_x$G were optimized. Subsequently, the single-point self-consistent calculations of Mn and N$_x$S$_x$G were performed. Finally, three CHGCAR files were processed by VASPKIT to obtain the output file (CHGDIFF.vasp) that could be opened by VESTA. The value of the isosurface was 0.007.

3. Results and discussion

3.1. Characterization of atomic Mn catalysts

The synthetic illustration of Mn-S-C, Mn-N-C and Mn-N/S-C is depicted in Fig. 1a. The morphology of Mn-N/S-C was studied by transmission electron microscope (TEM), displaying a typical folded nanosheet structure (Fig. 1b). To reveal the Mn sites, HAADF-STEM image was performed (Fig. 1c), showing that isolated single-atom Mn ions are immobilized into the graphene nanosheets and no obvious Mn-based nanoparticles or nanoclusters can be observed. From XRD patterns (Fig. S1), it can be further confirmed that no Mn-based nanoclusters were formed in the Mn-C, Mn-S-C, Mn-N-C, and Mn-N/S-C, since there
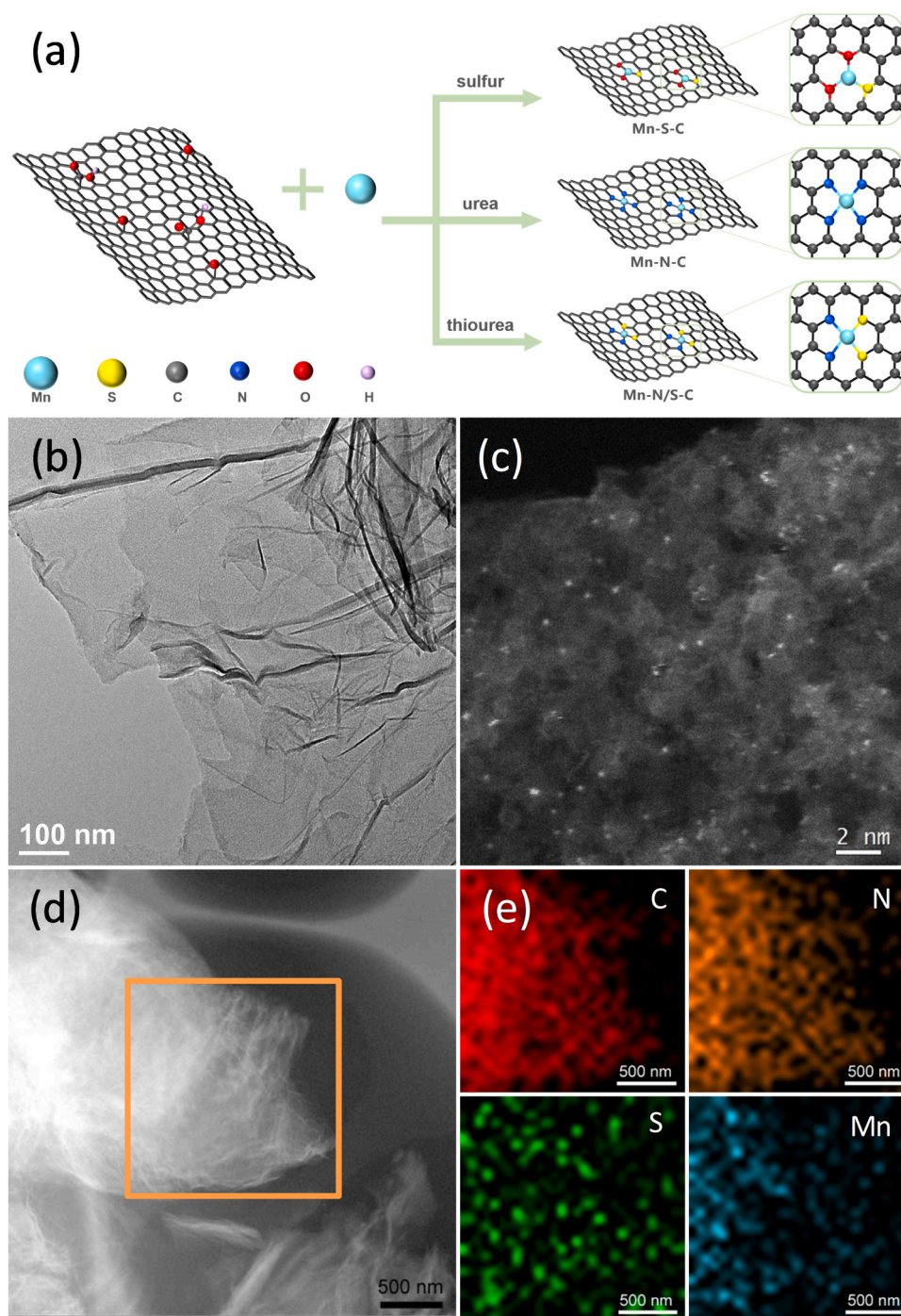
Fig. 1. (a) Synthetic illustration of Mn-S-C, Mn-N-C, and Mn-N/S-C. (b) TEM image of Mn-N/S-C. (c) HAADF-STEM image of Mn-N/S-C. (d) STEM image and (e) EDS elemental maps of Mn-N/S-C.

are no characteristic peaks due to these species. The EDS-STEM elemental mapping exhibits that C, O, N, S, and Mn elements are well dispersed on the graphene nanosheets (Fig. 1d,e).

The surface species on the Mn-C, Mn-S-C, Mn-N-C, and Mn-N/S-C catalysts were detected by XPS (Fig. 2a). As shown in Fig. 2b, the peak located at ca. 641.6 eV corresponds to Mn $3p_{3/2}$. However, due to different electronegativity and electron-donating effect of N, O and S elements, the peak position of Mn $3p_{3/2}$ for the Mn-C, Mn-S-C, Mn-N-C and Mn-N/S-C shifts slightly. With enhancing the electron-donating ability of the coordinated ligands, the peak of Mn $3p_{3/2}$ drifts to a smaller binding energy, leading to higher electron density around the Mn sites and lower oxidation valence of Mn. As a result, the peak

position value of Mn $3p_{3/2}$ for the Mn-N/S-C is the lowest due to the strong electron donation ability of N/S-co-coordination [34]. The N 1s peaks for Mn-N-C and Mn-N/S-C are deconvoluted into pyridinic N, Mn-N, pyrrolic N, graphitic N, and N-oxide (Fig. 2c) [35,36]. For the S element (Fig. 2d), the S $2p_{3/2}$ peaks for Mn-S-C and Mn-N/S-C are split into Mn-S (163.5 eV) and C-S (163.9 eV) [34,37]. Thus, the XPS results verify the formation of Mn-N and Mn-S bonds in the Mn-N/S-C.

The detailed atomic structural information of Mn-N/S-C was resolved by XAS. As demonstrated in Fig. 3a, the white line of Mn-N/S-C locates between Mn foil and Mn_3O_4 or MnO_2, indicating an oxidation valence state of $Mn^{\delta+}$ ($0 < \delta < 2.7$). The extended X-ray absorption fine structure (EXAFS) FT spectrum of Mn-N/S-C demonstrates a major peak
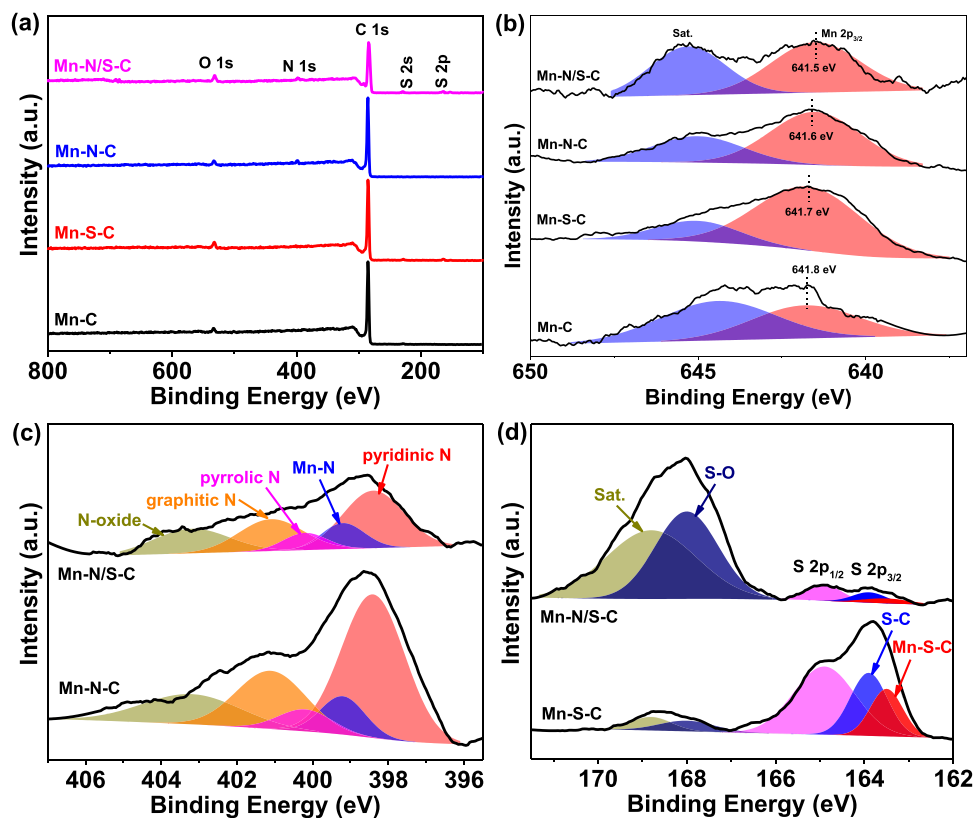
Fig. 2. (a) XPS survey spectra of Mn-C, Mn-S-C, Mn-N-C, and Mn-N/S-C. XPS spectra of (b) Mn 2p, (c) N 1 s, and (d) S 2p.
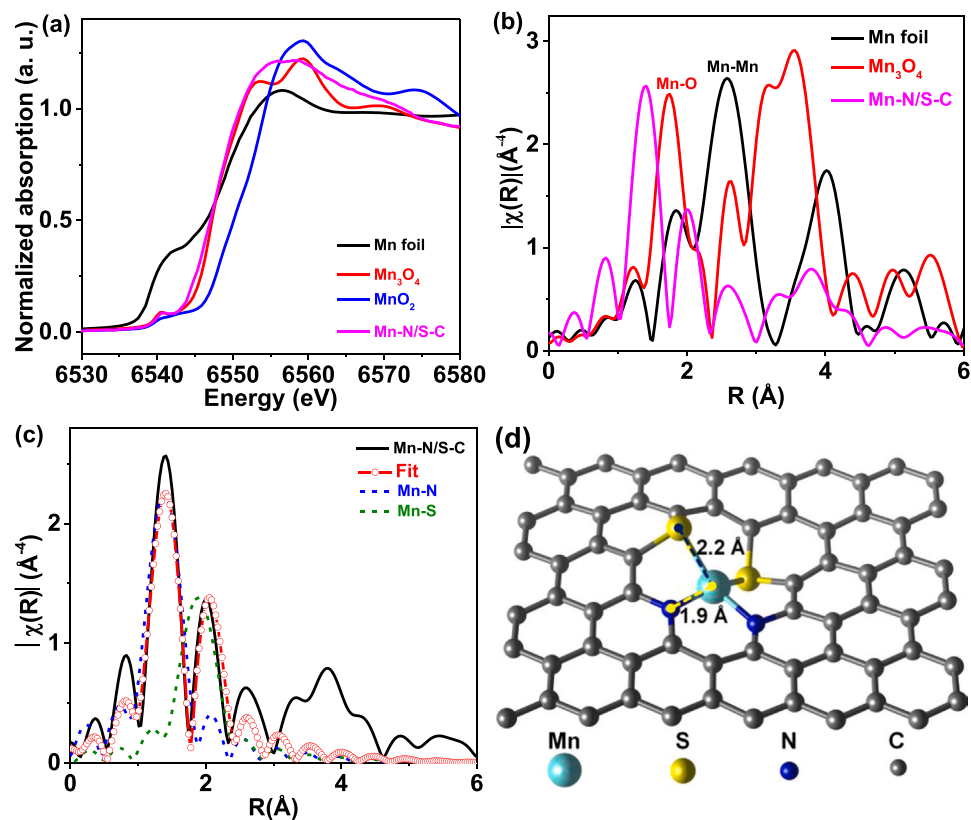

Fig. 3. (a) X-ray absorption near edge structure spectra at Mn K-edges of the Mn-N/S-C and referred samples. (b) FT-EXAFS spectra, (c) FT-EXAFS fitting spectrum. (d) Ortho-MnN$_2$S$_2$-G configuration.

at around 1.4 Å, which is different from Mn–O peak at 1.74 Å and Mn–Mn peak at 2.58 Å, corresponding to Mn–N bonding (Fig. 3b). Moreover, Mn-N/S-C demonstrates a moderate intensity peak at around 2.0 Å, corresponding to Mn–S bonding. The fitted EXAFS spectrum shows that the bond length of Mn–N is 1.90 ± 0.01 Å with coordination number of 2.0 ± 0.2 and the bond length of Mn–S is 2.33 ± 0.04 Å with coordination number of 1.7 ± 0.5 (Fig. 3c). The atomic structure of ortho-$Mn-N_2S_2$ moiety embedded into the graphene framework is depicted in Fig. 3d, which agrees with experimental structure.

3.2. ORR performance

The ORR performance of Mn-N/S-C was assessed in O_2-saturated 0.1 M KOH. For comparison, Mn-C, Mn-S-C, Mn-N-C and 20 wt% Pt/C were also assessed. From the CV curves (Fig. S2), the Mn-N/S-C presents a definite ORR peak at 0.91 V, which is absent in N_2-saturated solution, illustrating apparent ORR activity. Moreover, the peak potential of Mn-N/S-C is more positive than those of Mn-C (0.77 V), Mn-S-C (0.80 V), Mn-N-C (0.82 V), indicating favorable coordination of N and S ligands to Mn sites for ORR electrocatalysis. The onset potential of Mn-N/S-C is 1.013 V, superior to those of Mn-C (0.892 V), Mn-S-C (0.969 V), Mn-N-C (0.954 V) and Pt/C (0.951 V) (Fig. 4a). The $E_{1/2}$ of Mn-N/S-C is 0.91 V, superior to those of Mn-C (0.752 V), Mn-S-C (0.812 V), Mn-N-C (0.818 V), Pt/C (0.842 V) and most reported single-atom catalysts (Table S1). The Mn-N/S-C exhibits a low Tafel slope of 62 mV dec^{-1}, which is competitive with that of Pt/C (64 mV dec^{-1}) and smaller than those of Mn-C (108 mV dec^{-1}), Mn-S-C (99 mV dec^{-1}), Mn-N-C (97 mV dec^{-1}) (Fig. 4b), illustrating favorable ORR kinetics on the Mn-N/S-C. To further study the kinetics of Mn-N/S-C, the ORR polarization curves of Mn-N/S-C at different rotation speeds were collected (Fig. S3). The electron transfer number of Mn-N/S-C is determined to be ~3.95 according to the Koutecky-Levich plots, indicating a near-four-electron reduction route [38]. Further RRDE tests exhibits the n of

3.95, in good agreement with that derived from the K-L plots (Fig. 4c). The yields of H_2O_2 for Pt/C, Mn-C, Mn-S-C, Mn-N-C, and Mn-N/S-C were calculated from RRDE measurements (Fig. 4c). The H_2O_2 yield for the Mn-N/S-C is comparable to that for Pt/C, but obviously lower than those for Mn-C, Mn-S-C and Mn-N-C, testifying a main 4e⁻ reduction route on the Mn-N/S-C. The influence of Mn-doping content and annealing temperature on the ORR performance was investigated. As illustrated in Figs. S4-S5, the annealing temperature has a pivotal effect on the ORR performance and the optimal one is around 800 °C, while the optimum initial Mn content is 0.7 wt%. The appropriate annealing temperature favors the construction of high-performance active centers with reasonable Mn-N/S configuration while suitable Mn doping content maximizes the active site density.

The available active centers in the Mn-N/S-C were compared to those in Mn-C, Mn-S-C and Mn-N-C. As depicted in Figs. S6-S9, the electrochemical active surface area of Mn-N/S-C is determined to be 467 cm^{-2}, larger than those of Mn-C (222 cm^{-2}), Mn-S-C (286 cm^{-2}) and Mn-N-C (354 cm^{-2}), demonstrating more available active sites in the Mn-N/S-C for the ORR. The charge transfer ability of Mn-N/S-C was compared to that of Mn-C, Mn-S-C and Mn-N-C. As illustrated in Figs. S10, the charge transfer resistance of Mn-N/S-C is measured to be 4.0 Ω cm^2, slightly smaller than that of Mn-C (4.5 Ω cm^2), Mn-S-C (4.2 Ω cm^2) and Mn-N-C (4.1 Ω cm^2), indicating that N- and S- coordination to Mn sites can promote the charge transfer, thus accelerating ORR kinetics [39–41].

The stability of Mn-N/S-C and Pt/C was measured using the chronoamperometric test at 0.6 V (Fig. 4d). Significantly, 88.3 % of the original current can be reserved for Mn-N/S-C after 12 h, while only 70.0 % of the original current was kept for the Pt/C, demonstrating the superior electrochemical stability of the Mn-N/S-C. The structure of Mn-N/S-C after stability experiment was characterized by XRD (Fig. S11), showing that no metal-based nanoparticles were formed. The carbon monoxide poison effect was examined using the chronoamperometric response with the introduction of carbon monoxide (50 ml min^{-1})
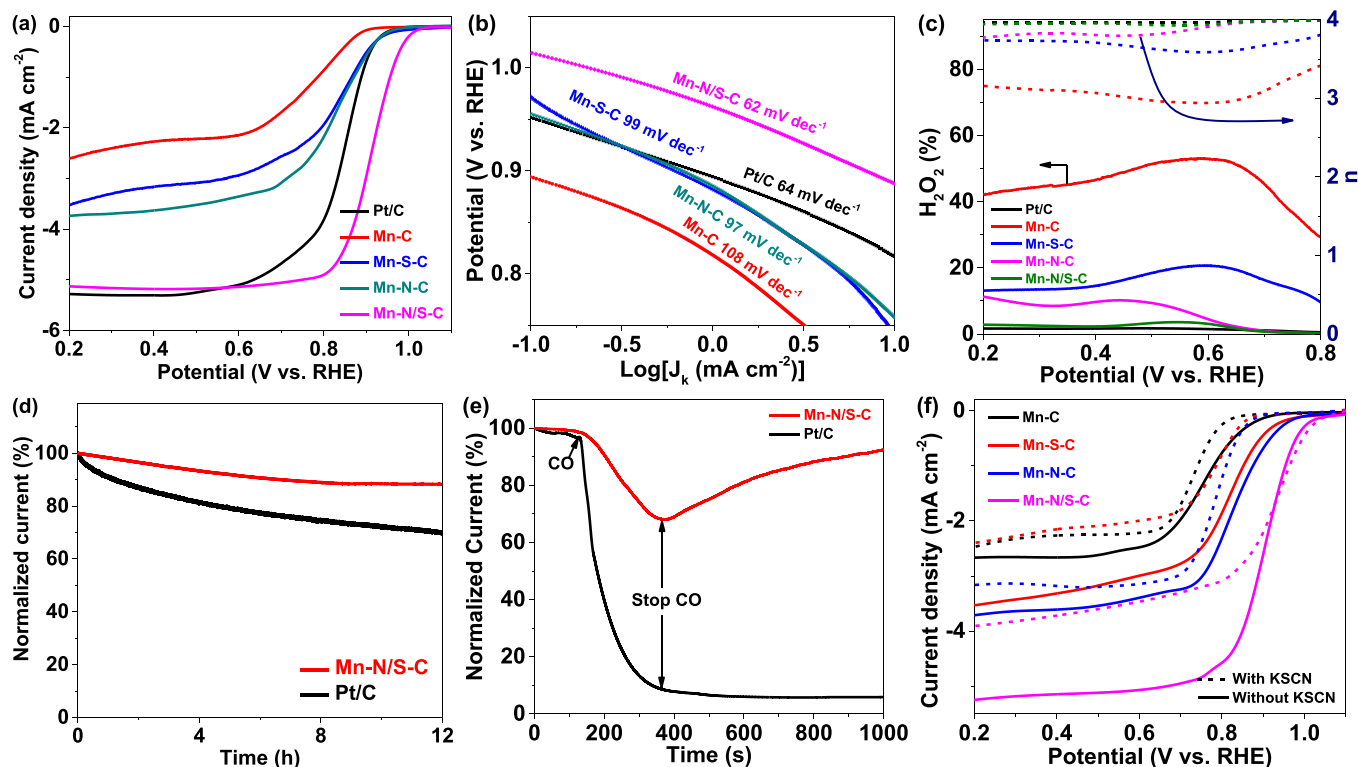

Fig. 4. (a) ORR polarization curves of Mn-C, Mn-S-C, Mn-N-C, Mn-N/S-C, and Pt/C. (b) Tafel plots. (c) Electron-transfer number (n) and H_2O_2 yield. (d) Chronoamperometric response of the Mn-N/S-C and Pt/C at 0.6 V. (e) Tolerance to carbon monoxide of Mn-N/S-C and Pt/C at 0.6 V. (f) ORR polarization curves for Mn-C, Mn-S-C, Mn-N-C, and Mn-N/S-C without (solid line) and with (dashed line) 10 mM KSCN.

(Fig. 4e). The current decreases with the introduction of CO for the Mn-N/S-C, while it can be recovered after stopping the introduction of CO, suggesting that the Mn-N/S-C has strong resistibility to CO poisoning. However, the current of Pt/C reduces greatly under the same conditions and it cannot be recovered even if stopping the addition of CO. The fuel crossover effect was evaluated by examining the chronoamperometric signal of the Mn-N/S-C and Pt/C with the introduction of methanol (Fig. S12). Slight current loss is observed for the Mn-N/S-C after introducing 3 M methanol, while more than 60% of current immediately drops for the Pt/C, indicating better methanol tolerance of Mn-N/S-C. To evaluate the role of Mn sites in the ORR, we carried out the KSCN poisoning test. As illustrated in Fig. 4f, the onset potential, the $E_{1/2}$ and the limited current density for Mn-C, Mn-S-C and Mn-N-C all decrease after the introduction of 10 mM KSCN into the electrolyte, implying that Mn ions were coordinated with SCN^-, leading to metal active site poisoning. However, for the Mn-N/S-C, the onset potential and the $E_{1/2}$ are not obviously influenced after adding the KSCN solution, indicating that the Mn sites in the Mn-N/S-C have strong resistivity to SCN^- poisoning, which is beneficial to the ORR electrocatalysis.

3.3. Zn-air battery performance

Considering the superior ORR performance of the Mn-N/S-C catalyst, we constructed it into a Zn–air battery (ZAB). Contrastive ZAB was also assembled by substituting Mn-N/S-C with Mn-N-C. As illustrated in Fig. 5a, Mn-N/S-C-based ZAB delivers a peak power density of 193 mW cm^{-2}, much larger than those of Mn-N-C-based ZAB (137 mW cm^{-2}) and most single-atom catalyst-based ZABs (Table S2). The open-circuit voltage of Mn-N/S-C-based ZAB can reach as high as 1.51 V (inset in Fig. 5b), much larger than that of Mn-N-C-based ZAB (1.45 V). The discharging plots at different current densities imply that the Mn-N-C-based ZAB can afford stable current output, which is

beneficial to electron devices (Fig. 5b). Furthermore, the specific capacity of Mn-N/S-C-based ZAB reaches a high energy density of 780.4 mAh g$_{Zn}^{-1}$ (Fig. 5c), higher than Mn-N-C-based ZAB (761.5 mAh g$_{Zn}^{-1}$). The rechargeability of Mn-N/S-C-based ZAB was then evaluated via charge–discharge cycles. As demonstrated in Fig. 5d, the Mn-N/S-C-based ZAB can be steadily charged and discharged for more than 750 cycles and 250 h at 5 mA cm^{-2}. The charge–discharge voltage gap increases by only 7 mV after 250 h, suggesting its excellent rechargeability. Overall, the electrochemical performance of Mn-N/S-C-based ZAB can be comparable to the best ZABs (Table S2).

3.4. Fuel cell performance

The AEMFC was fabricated using QPCBP-10 as the AEM, Mn-N-C or Mn-N/S-C as the cathode catalyst, and Pt-Ru/C as the anode catalyst (Fig. 6). The Mn-N/S-C-based MEA exhibits a higher open circuit potential value and higher current output than Mn-N-C-based MEA, indicating less ohmic loss, less mass transport loss and better AEMFC performance of Mn-N/S-C-based MEA. Additionally, the Mn-N/S-C-based MEA shows a peak power density of 247 mW cm^{-2} at 503 mA cm^{-2}, superior to Mn-N-C-based MEA (161 mW cm^{-2} at 373 mA cm^{-2}) and many SAC-based MEAs reported previously (Table S3), for instance, Cu SAC-based MEA (196 mW cm^{-2}) [42], Fe–N–CC-based MEA (123 mW cm^{-2}) [43], FeSiNC_50a-based MEA (208 mW cm^{-2}) [44], and C@PVI-(DFTPP)Fe-800-based MEA (104 mW cm^{-2}) [45], making the Mn-N/S-C a hopeful cathode for the AEMFC application.

3.5. Theoretical study on ORR mechanism

To explore the catalytic property difference of Mn-N$_x$S$_x$G at the atomic level, the density functional theory (DFT) calculation was
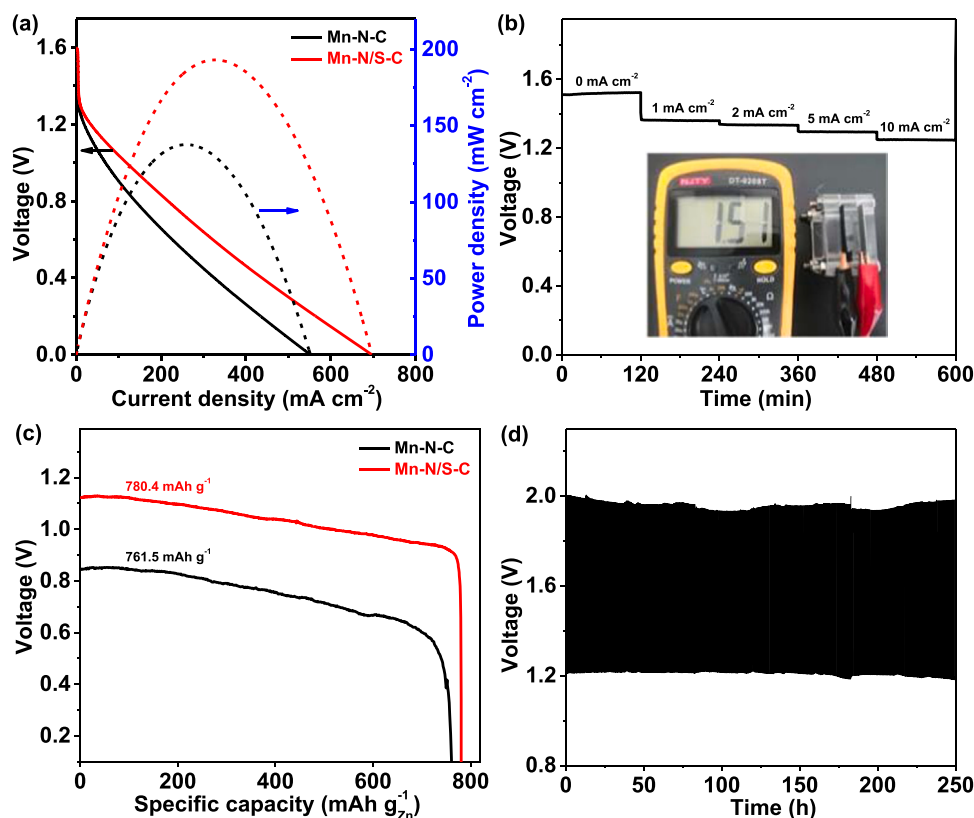

Fig. 5. (a) Discharging polarization and power density curves of Mn-N/S-C-based and Mn-N-C-based ZABs. (b) Discharging plateaus with different current densities of Mn-N/S-C-based battery. The inset is the digital picture of open-circuit voltage delivered by the Mn-N/S-C-based battery. (c) The specific capacity of Mn-N-C-based and Mn-N/S-C-based ZABs. (d) Galvanostatic cycling stability of Mn-N/S-C-based battery at 5 mA cm^{-2}.
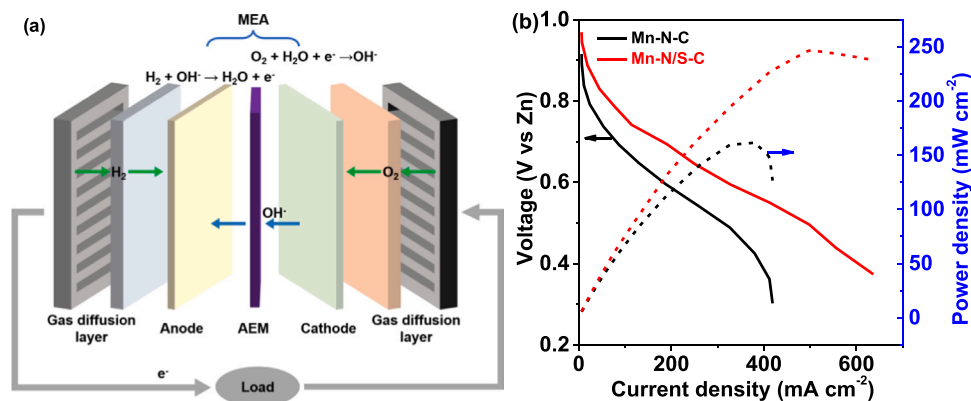
Fig. 6. (a) Schematic illustration of AEMFC. (b) Polarization plots of Mn-N-C-based and Mn-N/S-C-based H_2/O_2 fuel cells.

performed for the five catalytic systems. After screening by the energy evaluation, the five Mn-N_xS_xG models were established and optimized (Fig. 7a and Figs. S12-S16). The results showed that the catalytic sites of Mn-N_3SG, Mn-N_2S_2G, and Mn-NS_3G were nonplanar symmetric except for Mn-N_4G, due to the sulfur atom doping. The structures of Mn-N_4G and Mn-N_3SG were consistent with our previous work [34]. For the Mn-N_2S_2G, given the position of two sulfur atoms, two structure isomers of Mn-N_2S_2G were optimized, namely ortho-Mn-N_2S_2G and para-Mn-N_2S_2G. Subsequently, the reaction channels for the ORR and the intermediates are identified as the following: $* + O_2 \rightarrow OOH* \rightarrow O* \rightarrow OH* \rightarrow * + H_2O$, as shown in Fig. 7b and Figs. S13-S17. The results revealed that the intermediates are all energetically favored to adsorb the Mn, exhibiting stable configurations during the catalytic process. In the first step, the formation of OOH* on the catalytic surface is all exothermic reactions, suggesting that the five catalytic surfaces could form high-efficient adsorption for O_2. As for the generation of O*, the energies of catalytic systems further reduce, except for Mn-NS_3G. Mn-NS_3G has a low energy barrier (0.25 eV) to generate O*. Since the energy of OH* is smaller than those of O* and OOH* for Mn-N_4G, Mn-N_3SG and Mn-NS_3G, OH* is considered as the stable intermediate upon the absorption of OH, implying that the three catalytic systems are all exothermic from O* to OH*. In addition, ortho-Mn-N_2S_2G and para-Mn-N_2S_2G have the energy barriers of 0.16 and 0.12 eV in this step, respectively. In the final desorption stage, we found that the five catalytic surfaces all exhibit higher energy barriers than other reaction steps (Fig. 7b). During the ORR, the potential-determining step on these surfaces is OH* $\rightarrow$ * + H_2O and ortho-Mn-N_2S_2G exhibits the lowest energy barrier of 0.69 eV. Therefore, the ortho-Mn-N_2S_2G could catalyze the ORR more efficiently than other configurations, which matches with the experiments.

To deeply understanding the charge density differences of Mn in Mn-N_4G, Mn-N_3SG, ortho-Mn-N_2S_2G, para-Mn-N_2S_2G and Mn-NS_3G configurations, we explore the modulation of the local electronic structure of the central Mn by the doped S atoms (Fig. 8). The results show that due to the sulfur atom doping, the electron density of Mn in the ortho-Mn-N_2S_2G configuration increases significantly compared with Mn-N_4G. However, for the para-Mn-N_2S_2G configuration, the para-position of S atoms leads to less electron density of Mn, resulting in higher over-potential. The same is true for Mn-NS_3G. Therefore, the S atom doping and asymmetry of structure lead to higher catalytic activity of ortho-Mn-N_2S_2G. In addition, atomic charge calculation for Mn-N_xS_xG was carried out by Bader charge analysis. The results illustrate that the Bader charge (e) of Mn in ortho-Mn-N_2S_2G is higher than those of the other catalytic systems (Table S4), which matches with the results of charge density differences.

4. Conclusions

In summary, we developed a Mn-N/S-C electrocatalyst consisting of atomically dispersed Mn-N_2S_2 sites on 2D ultrathin graphene nanosheets. Owing to the large surface area, 2D ultrathin structure, and evenly-dispersed active centers, the Mn-N/S-C possessed high ORR performance with a positive $E_{1/2}$ of 0.91 V. The Mn-N/S-C based Zn−air battery could afford a high open-circuit voltage of 1.51 V, a peak power density of 193 mW cm^{-2} and long-term cycle stability. Moreover, Mn-N/S-C-based AEMFC can afford a peak power density of 247 mW cm^{-2}. DFT calculations revealed that the ortho-Mn-N_2S_2G active site is identified to activate the ORR, which is more active than the Mn-N_4G, Mn-N_3SG, para-Mn-N_2S_2G and Mn-NS_3G sites. The ORR rate-limiting steps on the ortho-Mn-N_2S_2G is predicted as the transformation of OH* to H_2O. The N-/S-co-coordinated strategy of constructing SACs represents a significant advance in developing high-
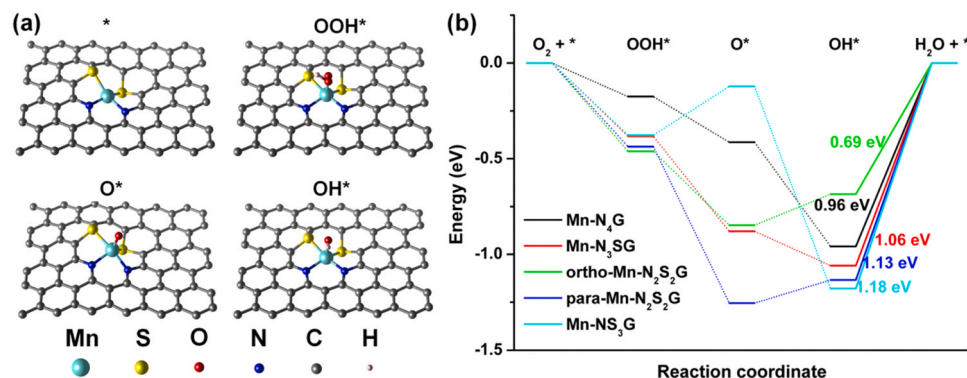

Fig. 7. (a) The optimized structures of ortho-Mn-N_2S_2G and three reaction intermediates. The reaction paths of free energy diagram for the ORR and on Mn-N_4G, Mn-N_3SG, ortho-Mn-N_2S_2G, para-Mn-N_2S_2G and Mn-NS_3G.
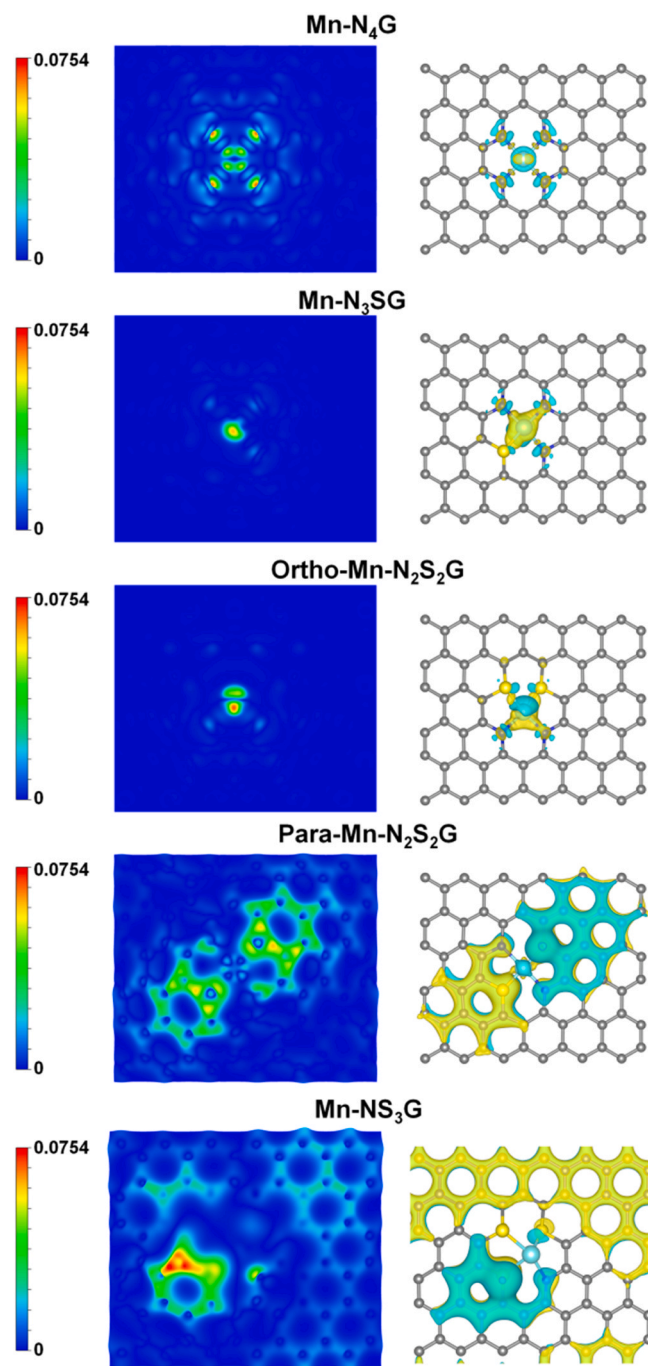
Fig. 8. The charge density differences of Mn in Mn-N$_4$G, Mn-N$_3$SG, ortho-Mn-N$_2$S$_2$G, para-Mn-N$_2$S$_2$G and Mn-NS$_3$G. Yellow and blue areas represent charge density accumulation and depletion in the 3D map, respectively.

performance ORR catalysts for energy-related fields.

CRediT authorship contribution statement

Xue Bai: Data curation, Investigation, Writing – original draft. **Yin Wang:** Investigation. **Jingyi Han:** Investigation. **Xiaodi Niu:** Investigation. **Jingqi Guan:** Conceptualization, Supervision, Writing – review and editing.

Declaration of Competing Interest

The authors declare that they have no known competing financial interests or personal relationships that could have appeared to influence the work reported in this paper.

Data availability

Data will be made available on request.

Acknowledgments

Appendix A. Supporting information

Supplementary data associated with this article can be found in the online version at doi:10.1016/j.apcatb.2023.122966.

References

[1] Y. Wang, F. Chu, J. Zeng, Q. Wang, T. Naren, Y. Li, Y. Cheng, Y. Lei, F. Wu, Single atom catalysts for fuel cells and rechargeable batteries: principles, advances, and opportunities, ACS Nano 15 (2021) 210–239, https://doi.org/10.1021/acsnano.0c08652.

[2] M. Wu, G. Zhang, W. Wang, H. Yang, D. Rawach, M. Chen, S. Sun, Electronic metal support interaction modulation of single-atom electrocatalysts for rechargeable zinc-air batteries, Small Methods 6 (2022), 2100947, https://doi.org/10.1002/smtd.202100947.

[3] Y. Yang, C.R. Peltier, R. Zeng, R. Schimmenti, Q. Li, X. Huang, Z. Yan, G. Potsi, R. Selhorst, X. Lu, W. Xu, M. Tader, A.V. Soudackov, H. Zhang, M. Krumov, E. Murray, P. Xu, J. Hitt, L. Xu, H.-Y. Ko, B.G. Ernst, C. Bundschu, A. Luo, D. Markovich, M. Hu, C. He, H. Wang, J. Fang, R.A. DiStasio Jr., L.F. Kourkoutis, A. Singer, K.J.T. Noonan, L. Xiao, L. Zhuang, B.S. Pivovar, P. Zelenay, E. Herrero, J. M. Feliu, J. Suntivich, E.P. Giannelis, S. Hammes-Schiffer, T. Arias, M. Mavrikakis, T.E. Mallouk, J.D. Brock, D.A. Muller, F.J. DiSalvo, G.W. Coates, H.D. Abruna, Electrocatalysis in alkaline media and alkaline membrane-based energy technologies, Chem. Rev. 122 (2022) 6117–6321, https://doi.org/10.1021/acs.chemrev.1c00331.

[4] Q. Zhang, J. Guan, Applications of atomically dispersed oxygen reduction catalysts in fuel cells and zinc-air batteries, Energy Environ. Mater. 4 (2021) 307–335, https://doi.org/10.1002/eem2.12128.

[5] P. Wang, D. Zhao, L. Yin, Two-dimensional matrices confining metal single atoms with enhanced electrochemical reaction kinetics for energy storage applications, Energy Environ. Sci. 14 (2021) 1794–1834, https://doi.org/10.1039/d0ee02651d.

[6] Y. Yang, P. Li, X. Zheng, W. Sun, S.X. Dou, T. Ma, H. Pan, Anion-exchange membrane water electrolyzers and fuel cells, Chem. Soc. Rev. 51 (2022) 9620–9693, https://doi.org/10.1039/d2cs00038e.

[7] J. Huang, L. Sementa, Z. Liu, G. Barcaro, M. Feng, E. Liu, L. Jiao, M. Xu, D. Leshchev, S.-J. Lee, M. Li, C. Wan, E. Zhu, Y. Liu, B. Peng, X. Duan, W. A. Goddard III, A. Fortunelli, Q. Jia, Y. Huang, Experimental Sabatier plot for predictive design of active and stable Pt-alloy oxygen reduction reaction catalysts, Nat. Catal. 5 (2022) 513–523, https://doi.org/10.1038/s41929-022-00797-0.

[8] L. Zhang, S. Jiang, W. Ma, Z. Zhou, Oxygen reduction reaction on Pt-based electrocatalysts: Four-electron vs. two-electron pathway, Chin. J. Catal. 43 (2022) 1433–1443, https://doi.org/10.1016/s1872-2067(21)63961-x.

[9] Q. Zhang, J. Guan, Applications of single-atom catalysts, Nano Res. 15 (2022) 38–70, https://doi.org/10.1007/s12274-021-3479-8.

[10] H. Niu, C. Xia, L. Huang, S. Zaman, T. Maiyalagan, W. Guo, B. You, B.Y. Xia, Rational design and synthesis of one-dimensional platinum-based nanostructures for oxygen-reduction electrocatalysis, Chin. J. Catal. 43 (2022) 1459–1472, https://doi.org/10.1016/s1872-2067(21)63862.

[11] Q. Zhang, J. Guan, Single-atom catalysts for electrocatalytic applications, Adv. Funct. Mater. 30 (2020), 2000768.

[12] Y. Zhang, J. Yang, R. Ge, J. Zhang, J.M. Cairney, Y. Li, M. Zhu, S. Li, W. Li, The effect of coordination environment on the activity and selectivity of single-atom catalysts, Coord. Chem. Rev. 461 (2022), 214493, https://doi.org/10.1016/j.ccr.2022.214493.

[13] F. Dong, M. Wu, Z. Chen, X. Liu, G. Zhang, J. Qiao, S. Sun, Atomically dispersed transition metal-nitrogen-carbon bifunctional oxygen electrocatalysts for zinc-air batteries: recent advances and future perspectives, Nano-Micro Lett. 14 (2022), 182001, https://doi.org/10.1007/s40820-021-00768-3.

[14] L. Deng, L. Qiu, R. Hu, L. Yao, Z. Zheng, X. Ren, Y. Li, C. He, Restricted diffusion preparation of fully-exposed Fe single-atom catalyst on carbon nanospheres for efficient oxygen reduction reaction, Appl. Catal., B 305 (2022), 121058, https://doi.org/10.1016/j.apcatb.2021.121058.

[15] R. Sgarbi, K. Kumar, V.A. Saveleva, L. Dubau, R. Chattot, V. Martin, M. Mermoux, P. Bordet, P. Glatzel, E.A. Ticianelli, F. Jaouen, F. Maillard, Electrochemical transformation of Fe-N-C catalysts into iron oxides in alkaline medium and its

impact on the oxygen reduction reaction activity, Appl. Catal., B 311 (2022), 121366, https://doi.org/10.1016/j.apcatb.2022.121366.

[16] C. Shao, L. Wu, Y. Wang, K. Qu, H. Chu, L. Sun, J. Ye, B. Li, X. Wang, Engineering asymmetric Fe coordination centers with hydroxyl adsorption for efficient and durable oxygen reduction catalysis, Appl. Catal., B 316 (2022), 121607, https://doi.org/10.1016/j.apcatb.2022.121607.

[17] S. Huang, Z. Qiao, P. Sun, K. Qiao, K. Pei, L. Yang, H. Xu, S. Wang, Y. Huang, Y. Yan, D. Cao, The strain induced synergistic catalysis of FeN4 and MnN3 dual-site catalysts for oxygen reduction in proton- /anion- exchange membrane fuel cells, Appl. Catal., B 317 (2022), 121770, https://doi.org/10.1016/j.apcatb.2022.121770.

[18] S. Lee, J. Choi, M. Kim, J. Park, M. Park, J. Cho, Material design and surface chemistry for advanced rechargeable zinc-air batteries, Chem. Sci. 13 (2022) 6159–6180, https://doi.org/10.1039/d1sc07212a.

[19] W.-J. Niu, J.-Z. He, B.-N. Gu, M.-C. Liu, Y.-L. Chueh, Opportunities and challenges in precise synthesis of transition metal single-atom supported by 2D materials as catalysts toward oxygen reduction reaction, Adv. Funct. Mater. 31 (2021), 2103558, https://doi.org/10.1002/adfm.202103558.

[20] J. Li, M. Chen, D.A. Cullen, S. Hwang, M. Wang, B. Li, K. Liu, S. Karakalos, M. Lucero, H. Zhang, C. Lei, H. Xu, G.E. Sterbinsky, Z. Feng, D. Su, K.L. More, G. Wang, Z. Wang, G. Wu, Atomically dispersed manganese catalysts for oxygen reduction in proton-exchange membrane fuel cells, Nat. Catal. 1 (2018) 935–945, https://doi.org/10.1038/s41929-018-0164-8.

[21] L. Bai, Z. Duan, X. Wen, J. Guan, Bifunctional atomic iron-based catalyst for oxygen electrode reactions, J. Catal. 378 (2019) 353–362, https://doi.org/10.1016/j.jcat.2019.09.009.

[22] Z. Yang, X. Wang, M. Zhu, X. Leng, W. Chen, W. Wang, Q. Xu, L.-M. Yang, Y. Wu, Structural revolution of atomically dispersed Mn sites dictates oxygen reduction performance, Nano Res. 14 (2021) 4512–4519, https://doi.org/10.1007/s12274-021-3823-z.

[23] X. Han, T. Zhang, W. Chen, B. Dong, G. Meng, L. Zheng, C. Yang, X. Sun, Z. Zhuang, D. Wang, A. Han, J. Liu, Mn-N4 oxygen reduction electrocatalyst: operando investigation of active sites and high performance in zinc–air battery, Adv. Energy Mater. 11 (2021) 2002753, https://doi.org/10.1002/aenm.202002753.

[24] X. Li, L. Xu, X. Ren, J. Gao, Y. Huang, B. Liu, Microenvironment modulation of single-atom catalysts and their roles in electrochemical energy conversion, Sci. Adv. 6 (2020), eabb6833, https://doi.org/10.1126/sciadv.abb6833.

[25] Y. Yang, K. Mao, S. Gao, H. Huang, G. Xia, Z. Lin, P. Jiang, C. Wang, H. Wang, Q. Chen, O-, N-atoms-coordinated Mn cofactors within a graphene framework as bioinspired oxygen reduction reaction electrocatalysts, Adv. Mater. 30 (2018), 1801732, https://doi.org/10.1002/adma.201801732.

[26] J. Zhang, Y. Zhao, C. Chen, Y.-C. Huang, C.-L. Dong, C.-J. Chen, R.-S. Liu, C. Wang, K. Yan, Y. Li, G. Wang, Tuning the coordination environment in single-atom catalysts to achieve highly efficient oxygen reduction reactions, J. Am. Chem. Soc. 141 (2019) 20118–20126, https://doi.org/10.1021/jacs.9b09352.

[27] H. Shang, X. Zhou, J. Dong, A. Li, X. Zhao, Q. Liu, Y. Lin, J. Pei, Z. Li, Z. Jiang, D. Zhou, L. Zheng, Y. Wang, J. Zhou, Z. Yang, R. Cao, R. Sarangi, T. Sun, X. Yang, X. Zheng, W. Yan, Z. Zhuang, J. Li, W. Chen, D. Wang, J. Zhang, Y. Li, Engineering unsymmetrically coordinated Cu-S1N3 single atom sites with enhanced oxygen reduction activity, Nat. Commun. 11 (2020) 3049, https://doi.org/10.1038/s41467-020-16848-8.

[28] Z. Chen, X. Su, J. Ding, N. Yang, W. Zuo, Q. He, Z. Wei, Q. Zhang, J. Huang, Y. Zhai, Boosting oxygen reduction reaction with Fe and Se dual-atom sites supported by nitrogen-doped porous carbon, Appl. Catal. B 308 (2022) 121206, https://doi.org/10.1016/j.apcatb.2022.121206.

[29] W. Xie, J. Li, Y. Song, S. Li, J. Li, M. Shao, Hierarchical carbon microtube@ nanotube core-shell structure for high-performance oxygen electrocatalysis and Zn-air battery, Nano-Micro Lett. 12 (2020) 97, https://doi.org/10.1007/s40820-020-00435-z.

[30] W. Yuan, L. Zeng, S. Jiang, C. Yuan, Q. He, J. Wang, Q. Liao, Z. Wei, High performance poly(carbazolyl aryl piperidinium) anion exchange membranes for alkaline fuel cells, J. Membr. Sci. 657 (2022), 120676, https://doi.org/10.1016/j.memsci.2022.120676.

[31] Hafner Kresse, Ab initio molecular dynamics for liquid metals, Phys. Rev. B: Condens. Matter 47 (1993) 558–561, https://doi.org/10.1103/PhysRevB.47.558.

[32] Hafner Kresse, Ab initio molecular-dynamics simulation of the liquid-metal-amorphous-semiconductor transition in germanium, Phys. Rev. B: Condens. Matter 49 (1994) 14251–14269, https://doi.org/10.1103/PhysRevB.49.14251.

[33] V. Wang, N. Xu, J.-C. Liu, G. Tang, W.-T. Geng, VASPKIT: A user-friendly interface facilitating high-throughput computing and analysis using VASP code, Comput. Phys. Commun. 267 (2021), 108033, https://doi.org/10.1016/j.cpc.2021.108033.

[34] X. Bai, L. Wang, B. Nan, T. Tang, X. Niu, J. Guan, Atomic manganese coordinated to nitrogen and sulfur for oxygen evolution, Nano Res. 15 (2022) 6019–6025, https://doi.org/10.1007/s12274-022-4293-7.

[35] M.D. Hossain, Z. Liu, M. Zhuang, X. Yan, G.-L. Xu, C.A. Gadre, A. Tyagi, I.H. Abidi, C.-J. Sun, H. Wong, A. Guda, Y. Hao, X. Pan, K. Amine, Z. Luo, Rational design of graphene-supported single atom catalysts for hydrogen evolution reaction, Adv. Energy Mater. 9 (2019) 1803689, https://doi.org/10.1002/aenm.201803689.

[36] J. Guan, Z. Duan, F. Zhang, S.D. Kelly, R. Si, M. Dupuis, Q. Huang, J.Q. Chen, C. Tang, C. Li, Water oxidation on a mononuclear manganese heterogeneous catalyst, Nat. Catal. 1 (2018) 870–877, https://doi.org/10.1038/s41929-018-0158-6.

[37] J. Xu, R. Li, C.-Q. Xu, R. Zeng, Z. Jiang, B. Mei, J. Li, D. Meng, J. Chen, Underpotential -deposition synthesis and in-line electrochemical analysis of single -atom copper electrocatalysts, Appl. Catal., B 289 (2021), 120028, https://doi.org/10.1016/j.apcatb.2021.120028.

[38] M. Chen, X. Li, F. Yang, B. Li, T. Stracensky, S. Karakalos, S. Mukerjee, Q. Jia, D. Su, G. Wang, G. Wu, H. Xu, Atomically dispersed MnN4 catalysts via environmentally benign aqueous synthesis for oxygen reduction: Mechanistic understanding of activity and stability improvements, ACS Catal. 10 (2020) 10523–10534, https://doi.org/10.1021/acscatal.0c02490.

[39] Z. Kong, T. Liu, K. Hou, L. Guan, Atomically dispersed Mn-N-4 electrocatalyst with high oxygen reduction reaction catalytic activity from metal-organic framework ZIF-8 by minimal-water-assisted mechanochemical synthesis, J. Mater. Chem. A 10 (2022) 2826–2834, https://doi.org/10.1039/d1ta09183b.

[40] L. Zong, F. Lu, W. Zhang, K. Fan, X. Chen, B. Johannessen, D. Qi, N.M. Bedford, M. Warren, C.U. Segre, P. Liu, L. Wang, H. Zhao, Atomically-dispersed Mn-(N-C-2)(2)(O-C-2)(2) sites on carbon for efficient oxygen reduction reaction, Energy Storage Mater. 49 (2022) 209–218, https://doi.org/10.1016/j.ensm.2022.04.016.

[41] L. Bai, Z. Duan, X. Wen, R. Si, J. Guan, Atomically dispersed manganese-based catalysts for efficient catalysis of oxygen reduction reaction, Appl. Catal. B 257 (2019), 117930, https://doi.org/10.1016/j.apcatb.2019.117930.

[42] L. Cui, L. Cui, Z. Li, J. Zhang, H. Wang, S. Lu, Y. Xiang, A copper single-atom catalyst towards efficient and durable oxygen reduction for fuel cells, J. Mater. Chem. A 7 (2019) 16690–16695, https://doi.org/10.1039/C9TA03518D.

[43] G.A. Ferrero, K. Preuss, A. Marinovic, A.B. Jorge, N. Mansor, D.J.L. Brett, A. B. Fuertes, M. Sevilla, M.-M. Titirici, Fe–N-doped carbon capsules with outstanding electrochemical performance and stability for the oxygen reduction reaction in both acid and alkaline conditions, ACS Nano 10 (2016) 5922–5932, https://doi.org/10.1021/acsnano.6b01247.

[44] H.S. Kim, C.H. Lee, J.-H. Jang, M.S. Kang, H. Jin, K.-S. Lee, S.U. Lee, S.J. Yoo, W. C. Yoo, Single-atom oxygen reduction reaction electrocatalysts of Fe, Si, and N co-doped carbon with 3D interconnected mesoporosity, J. Mater. Chem. A 9 (2021) 4297–4309, https://doi.org/10.1039/D0TA11208A.

[45] Y.-M. Zhao, P.-C. Zhang, C. Xu, X.-Y. Zhou, L.-M. Liao, P.-J. Wei, E. Liu, H. Chen, Q. He, J.-G. Liu, Design and preparation of Fe-N-5 catalytic sites in single-atom catalysts for enhancing the oxygen reduction reaction in fuel cells, ACS Appl. Mater. Interfaces 12 (2020) 17334–17342, https://doi.org/10.1021/acsami.9b20711.